Hollmann, E.M.; Commaux, N.; Eidietis, N.W.; Lasnier, C.J.; Rudakov, D.L.; Shiraki, D.; Cooper, C.; Martin-Solis, J.R.; Parks, P.B.; Paz-Soldan, C. (2017). Study of Z scaling of runaway electron plateau final loss energy deposition into wall of DIII-D. *Physics of Plasmas*, 24(7), 62505, [10] p.

DOI: http://dx.doi.org/10.1063/1.4985086

Study of Z scaling of runaway electron plateau final loss energy deposition into wall of DIII-D

E. M. Hollmann,[1] N. Commaux,[2] N. W. Eidietis,[3] C. J. Lasnier,[4] D. L. Rudakov,[1] D. Shiraki,[2] C. Cooper,[5] J. R. Martin-Solis,[6] P. B. Parks,[3] and C. Paz-Soldan[3]
[1]*Center for Energy Research, University of California – San Diego, La Jolla, California 92093-0417, USA*
[2]*Oak Ridge National Laboratory, PO Box 2008, Oak Ridge, Tennessee 37831, USA*
[3]*General Atomics, PO Box 85608, San Diego, California, USA*
[4]*Lawrence Livermore National Laboratory, PO Box 808, Livermore, California 94551-0808, USA*
[5]*Oak Ridge Associated Universities, PO Box 117, Oak Ridge, Tennessee 37831-0117, USA*
[6]*Universidad Carlos III de Madrid, Avenida de la Universidad 30, 28911 Madrid, Spain*

(Received 6 April 2017; accepted 15 May 2017; published online 12 June 2017)

Controlled runaway electron (RE) plateau-wall strikes with different initial impurity levels are used to study the effect of background plasma ion charge Z (resistivity) on RE-wall loss dynamics. It is found that Joule heating (magnetic to kinetic energy conversion) during the final loss does not go up monotonically with increasing Z but peaks at intermediate $Z \sim 6$. Joule heating and overall time scales of the RE final loss are found to be reasonably well-described by a basic 0D coupled-circuit model, with only the loss time as a free parameter. This loss time is found to be fairly well correlated with the avalanche time, possibly suggesting that the RE final loss rate is limited by the avalanche rate. First attempts at measuring total energy deposition to the vessel walls by REs during the final loss are made. At higher plasma impurity levels $Z > 5$, energy deposition to the wall appears to be consistent with modeling, at least within the large uncertainties of the measurement. At low impurity levels $Z < 5$, however, local energy deposition appears around 5–20× less than expected, suggesting that the RE energy dissipation at low Z is not fully understood. *Published by AIP Publishing.*
[http://dx.doi.org/10.1063/1.4985086]

I. INTRODUCTION

Runaway electrons (REs) can form in tokamaks during startup or disruptions and can be a concern because of their ability to cause localized damage to in-vessel components.[1,2] In future large tokamaks like ITER, disruption REs could be a yet more serious concern and could potentially reduce machine operational lifetime,[3] so efforts are underway to study methods of disruption RE avoidance and mitigation.[4] Presently, it is thought that massive injection of high-Z impurities is a promising method for dissipating large post-disruption RE beams (RE plateaus), with very rapid reduction of RE plateau energy seen in DIII-D.[5] It has been pointed out, however, that increased plasma resistivity could tend to result in increased conversion of magnetic to kinetic energy during the wall strike, possibly resulting in greater net localized energy deposition, despite increased initial dissipation of kinetic energy.[6] It is therefore important to study the dynamics of RE plateau energy deposition to the wall as a function of plasma impurity content, in order to best design the RE mitigation system for ITER.

Measuring the RE energy deposition to the tokamak wall is challenging because of the spatially localized deposition, fast time scales, and high kinetic energy (MeV+) of the REs. Soft x-ray (SXR) array data in JET showed that the RE plateau tends to maintain a fairly narrow (minor radius $a \sim 0.5$ m) beam as it moves vertically to the wall.[7] This fairly small RE plateau minor radius is consistent with later DIII-D observations (assuming some machine size scaling), which found a minor radius $a \sim 0.2$–0.4 m based on final loss onset times and $a \sim 0.2$ m based on the FWHM of reconstructed SXR emissivities.[5] Hard x-ray (HXR) array data in DIII-D indicated a significant toroidal structure in the RE plateau wall strike, and this was attributed to MHD (kink) mode formation during the wall strike.[8] In TEXTOR, calorimeter and scintillator probes were used to measure the local energy of plateau REs striking the wall; mean energies of order several MeV were measured and RE plateau magnetic-kinetic energy conversions of up to nearly 30% were estimated.[9]

The expectation that RE plateau energy will be dominated by magnetic energy in ITER and the resulting importance of RE Joule heating (magnetic-kinetic energy conversion) during the final wall strike was first pointed out fairly early in the ITER design.[10] Initial simulations for ITER suggested a fairly modest (∼10%) conversion of magnetic energy to kinetic energy during the RE plateau final wall strike in ITER.[11] Experimentally, magnetics data were used to estimate the Joule heating in JET for uncontrolled RE plateau-wall strikes.[12] A model was developed to extrapolate these results to ITER and a higher magnetic—kinetic energy conversion fraction of 40% was arrived at for typical loss timescales. Data were gathered on uncontrolled RE-wall strikes in JET, DIII-D, and FTU; based on trends in uncalibrated HXR and photoneutron signals, evidence for significant (up to 10×) increase in net kinetic energy deposition to the wall due to magnetic energy conversion during the RE-wall strike was reported.[6]

In addition to RE Joule heating, a very important parameter needed for predicting RE damage for ITER is the RE heating footprint. IR images of the RE-wall strike region

gave a poloidal scale of order 10 cm in JET;[13] this was then used (assuming a 40% magnetic-kinetic energy conversion) to estimate a rough limit of 2 MA allowing for a RE plateau-wall strike in ITER.[4] More recent simulations have been performed using the actual ITER first wall panel geometry, which suggest that 2 MA may still be unacceptably high, depending on the degree of toroidal localization of the RE heating.[14]

The work presented here adds to the present understanding of the RE plateau-wall interaction in several areas. First, controlled RE vertical loss experiments with different levels of plateau impurity concentration are presented. These remove the large scatter in loss time of previous uncontrolled RE-wall loss experiments, allowing study of the trends resulting from plasma impurity content. It is found that the RE loss timescale tends to be of order the avalanche timescale. Additionally, first attempts (using HXR and IR data) are made to determine the energy deposited into the wall by the REs during the wall strike, which is the sum of the initial kinetic energy plus the Joule heating during the final loss minus any non-local energy loss (e.g., radiation) during the final loss. Within the fairly large experimental uncertainty, the results appear to be consistent with calculations for medium to high Z RE beams ($Z > 5$) but about 5–20× lower than expected at lower $Z < 5$. Consistent with JET results,[12] radiated power loss during the final loss appears to generally be fairly negligible. First attempts are made to measure the size of the RE heating footprint on the wall of DIII-D. From HXR scintillator data, the footprint appears somewhat large (covering a toroidal range of about 180°); however, the toroidal resolution of this method is quite coarse and will therefore average over small structures in the RE heat deposition. The phase of the HXR-inferred heat deposition is not random but appears to trend toward two toroidal angles. IR imaging indicates that conducted heat loads within the IR camera field of view (which covers about 60° toroidally) are fairly localized, to about a 10 cm wide region; however, this may be influenced by local non-uniformities in metal deposits in the floor.

II. EXPERIMENTAL SETUP

The experiments described here were performed in the DIII-D tokamak.[15] An experimental schematic showing key diagnostics is shown in Fig. 1. RE plateau-producing disruptions are induced with rapid (∼200 m/s) injection of small (OD ∼ 2 mm, volume ∼15 Torr-L) frozen argon pellets. The impurity content of the resulting RE plateau is modified by massive gas injection (MGI) of Ar, He, or D_2 gas from a fast gas valve. Line-integrated total electron density is measured with four interferometer view chords. Total radiation is measured with a foil bolometer. Soft x-ray (SXR) emission is measured with a poloidal fan of SXR view chords. Visible line emission is measured with a visible survey spectrometer. Hard x-ray (HXR) emission is measured with an array of 20 HXR scintillators located around the machine toroidally and poloidally. Infra-red (IR) imaging is done in the 3–5 μm range through a periscope viewing the entire plasma cross section over a toroidal region of about 60°. Magnetic signals and toroidal loop voltage are measured with coils mounted both external and internal to the vacuum vessel.

A time history of a typical experiment is shown in Fig. 2. An L-mode, electron cyclotron wave (gyrotron) heated inner wall-limited target plasma with a plasma current of 1.2 MA is shut down at time $t = 1200$ ms with an Ar pellet, leading to the formation of a RE plateau. The RE plateau current channel is captured, centered, and current-regulated to 275 kA by the plasma control system. Then, at $t = 1450$ ms, 300 Torr-L of helium MGI is fired into the RE plateau, resulting in a drop in HXR emission, Fig. 2(b), and a rise in electron density, Fig. 2(d). Also, the plasma control system is used to give the current channel a fixed-amplitude downward "kick," resulting in a slow downward drift of the current channel, Fig. 2(c), and wall impact and final loss at around t = 1650 ms.

III. RE FINAL LOSS TIME SCALES AND 0D COUPLED-CIRCUIT MODEL

A zoomed view of toroidal current time traces from a typical final loss event is shown in Fig. 3(a). The total plasma current I_P is measured using a poloidal array of poloidal magnetic field loops inside the conducting wall. The wall current I_{Wall} is measured using a Rogowski loop external to the conducting wall to measure the total toroidal

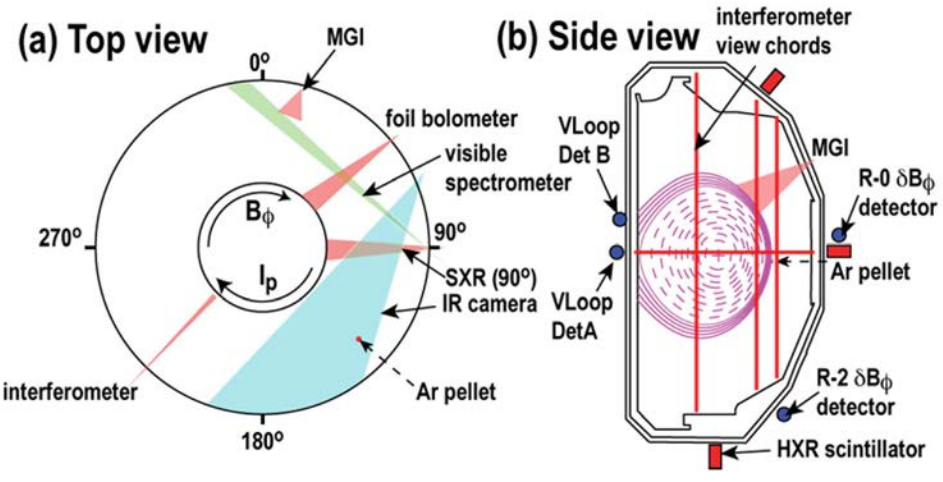

FIG. 1. Schematic of key DIII-D diagnostics and injectors showing (a) top view and (b) side view.

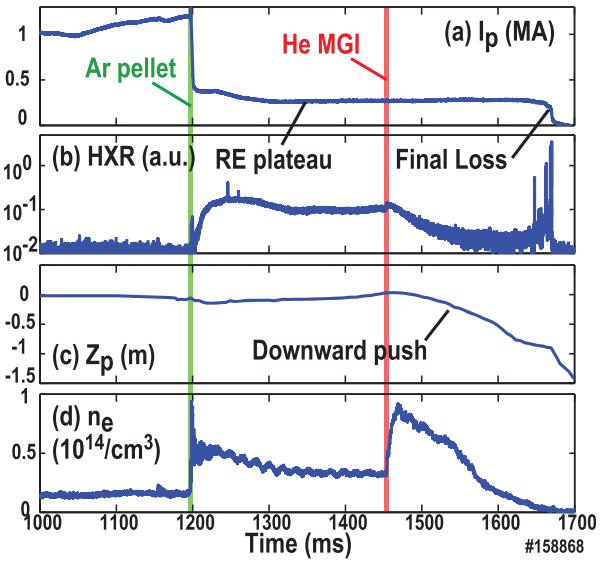

FIG. 2. Overview of typical experiment time sequence showing (a) plasma current, (b) HXR signal, (c) plasma vertical position, and (d) electron density.

current; subtracting plasma current from this gives wall current I_{Wall}. The ohmic plasma current I_Ω is estimated by assuming that toroidal ohmic current is proportional to poloidal halo current I_{Halo} measured by tile halo current monitors, as might be expected if ohmic current is dominantly in the open flux surface "scrape-off" region of the current channel

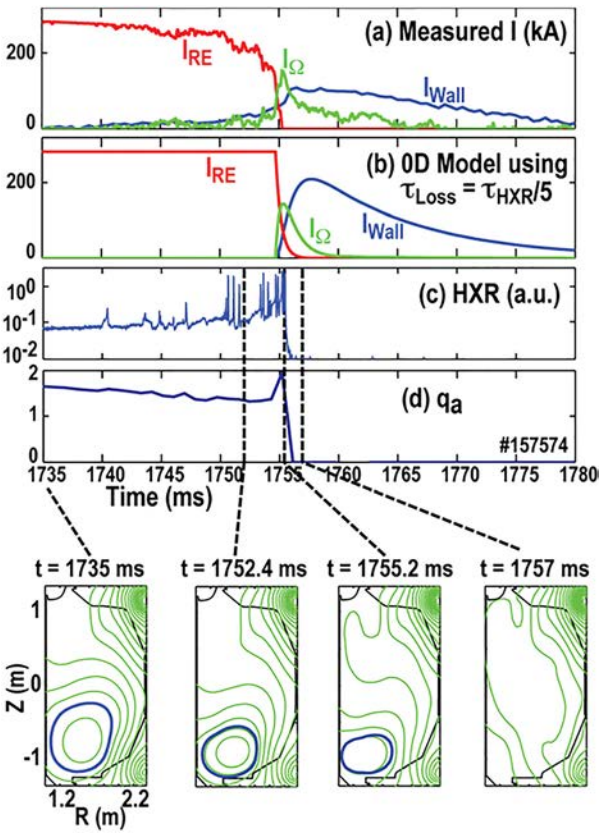

FIG. 3. Zoomed time traces of final loss event showing: (a) measured toroidal currents in wall and plasma, (b) OD model toroidal currents, (c) HXR signals, and (d) edge safety factor. The lower 4 panes show JFIT current reconstructions showing the last closed flux surface (blue) at four time steps.

where REs have been lost (and ignoring changes in edge safety factor q_a during the final loss). Using $I_P = I_\Omega + I_{RE}$, the scale factor for I_Ω is then obtained by requiring that I_{RE} goes to zero when the HXR signals, Fig. 3(c), go to zero.

The measured toroidal currents of Fig. 3(a) can be seen to be reasonably consistent with a 0D coupled circuit model.[6] To illustrate this, Fig. 3(b) shows toroidal currents calculated from the 0D model. For simplicity, RE current is assumed to be lost to the wall exponentially during the final loss event on a time scale τ_{Loss}. The RE current can then be integrated forward in time from the initial RE current using $\frac{\partial I_{RE}}{\partial t} = I_{RE}\left(\frac{1}{\tau_{Aval}} - \frac{1}{\tau_{Loss}}\right)$, where τ_{Aval} is the avalanche time scale. In the 0D model, the Ohmic plasma current can then be calculated using $\frac{\partial I_\Omega}{\partial t} = -I_\Omega/\tau_\Omega + \alpha_L(I_{Wall}/\tau_{Wall}) - \left(\frac{\partial I_{RE}}{\partial t}\right)$, while wall current can be calculated using $\frac{\partial I_{\mathrm{Wall}}}{\partial t} = I_\Omega/\tau_\Omega - (1+\alpha_L)(I_{Wall}/\tau_{Wall})$. $\alpha_L \approx 0.7$ is the ratio of internal to external inductances (estimated from the beam radius from SXR and the beam position relative to the wall from magnetics), τ_Ω is the Ohmic plasma decay time (estimated from the initial measured internal current decay rate after the total loss of RE current), and $\tau_{Wall} \approx 8$ ms is the wall time.

Figures 3(a) and 3(b) show that the 0D model toroidal currents are found to agree with the experiments reasonably well. Here, a loss time $\tau_{Loss} = \tau_{HXR}/5$ is used, where τ_{HXR} is the time scale for HXR final loss flashes, obtained from tanh fits to the time-integrated wall-emitted HXR signal, as shown in Fig. 4. It is not unexpected that τ_{Loss} should be somewhat shorter than τ_{HXR}, since the tanh fits to the entire RE current loss, while the faster slope of the rapid final decay of RE current is most important for wall and Ohmic current

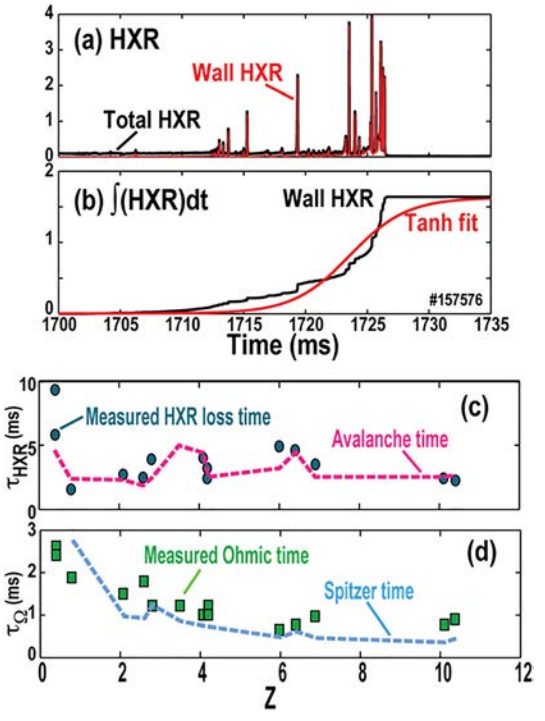

FIG. 4. (a) Total HXR signal and HXR signal from wall only during final loss and (b) tanh fit to integrated HXR signal to estimate RE loss time scale. (c) Measured HXR loss time and predicted avalanche time; and (d) measured Ohmic decay time and Spitzer resistivity time scale as a function of Z.

generation. The wall-emitted HXR signal, Fig. 4(a), is estimated from the total HXR signal by assuming that plasma HXR emission is proportional to RE current and that all measured HXRs originate from the plasma (not the wall) before the final loss starts. Figure 4(b) shows a tanh fit to integrated wall HXR emission, and Fig. 4(c) shows that τ_{HXR} is found to be reasonably well correlated with the theoretical avalanche time scale (the time scale for growth of secondary REs due to collisions between REs and background cold electrons) $\tau_{Aval} \approx \left(\frac{m_e c}{eE_\phi}\right) \ln\Lambda \sqrt{3(Z+5)/\pi}$; this is averaged over the final loss event for Fig. 4(c). Z and $\ln\Lambda$ used here are not the standard Coulomb collision quantities; instead, mean values appropriate for relativistic incoming electrons including free and bound target electrons are used. Free and bound electron densities are calculated from interferometers and spectroscopically measured argon ion densities.[16]

The background plasma Ohmic time scale τ_Ω is found to be reasonably well described by Spitzer resistivity, as shown by the dashed curve in Fig. 4(d). This curve is made by assuming $\tau_\Omega \approx L_{int}/R_\phi$, where L_{int} is the RE beam internal inductance (L_{ext} is neglected since $\tau_\Omega \ll \tau_{Wall}$) and R_ϕ is the toroidal resistance, calculated using the standard Spitzer plasma resistivity η. The Ohmic plasma charge state and electron temperature used to calculate η are estimated by assuming that the fractional impurity content (Ar, He, etc.) of the Ohmic plasma is the same as the pre-loss RE beam and that the temperature of the Ohmic plasma can be estimated by balancing Joule heating of the Ohmic plasma $E_\phi J_\Omega$ with power loss via line radiation. Points and curves in Figs. 4(c) and 4(d) are calculated at the same discrete Z points, but points are missing in some cases due to diagnostic problems e.g., due to unacquired spectroscopic data.

The toroidal electric field E_ϕ inside the RE beam during the final loss is estimated using an externally measured loop voltage (detector A in Fig. 1) plus a parabolic current profile approximation. In this approximation, the central loop voltage V_0 (in-beam loop voltage averaged across the RE beam) is given by: $V_0 \approx V_A - \frac{3}{4}\mu_0 R_0 \frac{\partial I_P}{\partial t}$, where V_A is the edge loop voltage; this is shown as a function of time by a dashed blue curve in Fig. 5(a). The external loop voltages measured at detectors A and B can be reasonably well predicted by JFIT, as shown in Fig. 5(a). JFIT can also be used to estimate V_0, shown by the black curve in Fig. 5(b). It can be seen that the JFIT loop voltage seems to be reasonably accurate but does not capture fast events, justifying the use of the faster parabolic I_P approximation [red curve in Fig. 5(b)] to better capture the dynamics of the final loss. The loop voltage profile may not actually be parabolic, but the precise radial structure of the toroidal electric field is unknown. Simulations of a slow "scrape off" of RE current during the final loss indicate the formation of a hollow radial profile of current and electric field;[11] however, these simulations do not include the current broadening effect of reconnection events, island overlap, etc., and there are no existing measurements to validate these simulations.

IV. HXR SPIKES DURING RE FINAL LOSS

Fast magnetics data suggest that the HXR spikes may result from internal MHD reconnection events analogous to those seen following the thermal quench (TQ) of normal disruptions. Figure 6 shows a further zoom of the data of Fig. 3 showing only three of the HXR flashes. Figure 6(d) shows toroidal contours of the HXR flashes (from the upper array). It can be seen that the first large HXR flash at around

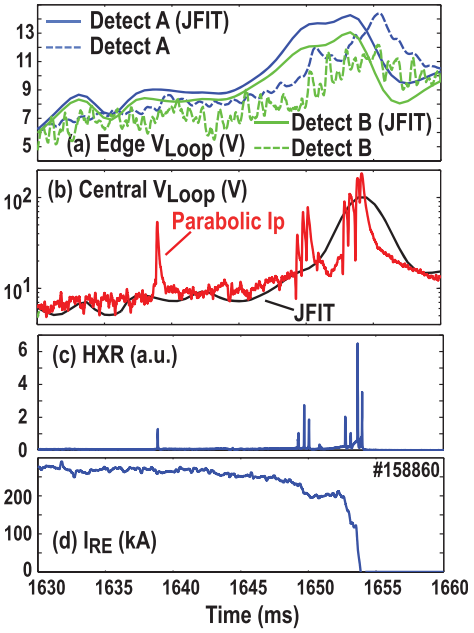

FIG. 5. (a) Edge toroidal loop voltage during final loss event showing reconstructed (JFIT) and measured loop voltage at detectors A and B; (b) central toroidal loop voltage from JFIT and parabolic I_p approximation; (c) HXR signals; and (d) RE current as a function of time.

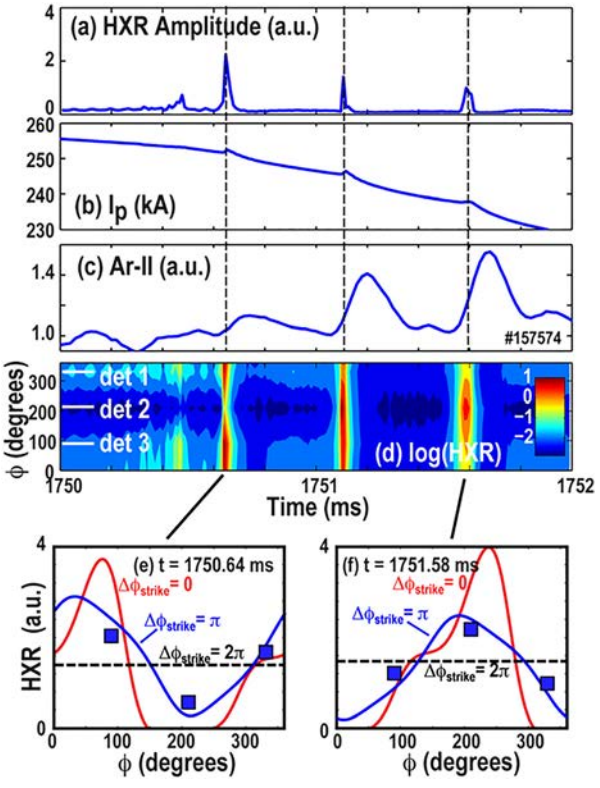

FIG. 6. Highly zoomed time traces of three final loss spikes showing (a) HXR amplitude, (b) plasma current, (c) Ar-II brightness, (d) toroidal structure of HXR signals, and (e) and (f) top-hat model fits to the toroidal structure of HXR signals during two different final loss spikes.

t = 1750 ms has a peak phase of around 20°, but the subsequent two large flashes have peak phases of around 200°, so about 180° apart. The fast internal poloidal array of magnetic pickup loops typically does not show an easily resolved poloidal mode number (probably because the current channel is close to the lower divertor and therefore the signal is quite different in amplitude at different poloidal locations), but integrating poloidally does clearly reveal fast spikes in the toroidal current coincident with the HXR flashes, Fig. 6(b), consistent with internal reconnection events in the current channel causing radial spreading of the current profile. The HXR flashes are extremely narrow, 10 μs–100 μs; the precise mechanism for this very rapid release of REs into the wall has not been identified yet, but one possibility suggested recently is that a stochastic annulus bounded by good flux surfaces could form during the final loss. Breaking the good surfaces could then result in a very rapid loss of significant REs on a time scale of 10 μs.[17] Figure 6(c) shows fast Ar-II line emission brightness as a function of time from a view chord which passes through the current channel. It can be seen that there are spikes in Ar-II emission following the HXR spikes; this is consistent with an increase in Ohmic current and resulting increased radiative dissipation following the RE current loss during HXR spikes. In Figs. 6(e) and 6(f), curves show model fits to the measured toroidal structure of the HXR signals at two spikes. Despite the very coarse toroidal resolution (only three data points), it can be seen that the measured toroidal structure can be reasonably well-fit assuming a RE deposition region $\Delta\phi_{Strike} \approx \pi$, i.e., wrapping around about half the tokamak. This model assumes a simple top-hat toroidal profile of energy deposition. HXR bremsstrahlung from RE impact is modeled using previous triply-differential simulations of bremsstrahlung,[18] parametrized analytically as done in the GEANT4 code.[19] The x-ray signal modeling includes energy sensitivity, geometry, and shielding structure of the HXR detectors. The energy distribution of REs during the final strike is estimated with kinetic (test particle) simulations, as will be described later.

The peak phases shown in Figs. 6(e) and 6(f) for HXR data are found to be fairly typical, suggesting that the RE current channel forms a MHD mode which locks to the DIII-D wall with preferred phase. This can be seen in Fig. 7 where histograms of peak HXR toroidal phase are plotted for (a) forward I_p and (b) reverse I_p shots. Forward and reverse I_p are separated because the different magnetic helicities might easily be expected to have different preferred wall strike locations. Data for many shots and many HXR final loss spikes are included, demonstrating that the final loss phase is not random. The HXR histograms in Fig. 7 show the expected actual peak phase of the RE-wall strike; this is different by of order 60° from the measured peak phase due to the forward-beaming of the HXRs from the wall strike point. It is not clear from the present analysis if the observed structure corresponds to a toroidally varying $n = 2$ mode or a $n = 1$ mode which is changing phase between strikes. This toroidal structure and variation of HXR phase will be studied further in future work; here, for the purposes of estimating total energy deposition, toroidally averaged HXR signals are used.

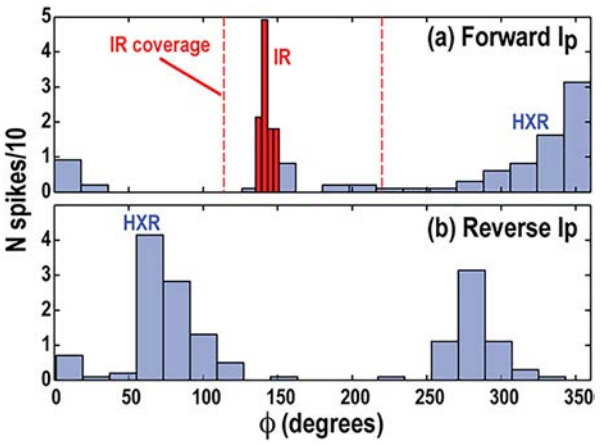

FIG. 7. Histograms of peak heat loads as a function of toroidal angle ϕ from HXR and IR diagnostics for (a) forward I_p and (b) reverse I_p shots. HXR histograms count HXR spikes (/10) while IR histogram counts shots.

V. IR THERMOGRAPHY

To complement the HXR measurements, it was attempted to measure RE-wall strike heat loads using IR thermography. Interpretation of IR images in these experiments is complicated by the presence of plasma IR emission and by unknown wall composition, so a large number of assumptions are necessary to make analysis tractable. A sample IR image of the lower divertor floor at the end of a RE final strike into the lower divertor is shown in Fig. 8(a). IR brightness is converted to a surface temperature assuming that the IR emissivity is dominated by graphite. Different regions of the divertor show markedly different time evolution during the final loss: some regions show a very slow (~100 ms) rise in IR signal, followed by a rapid (several ms) drop during the final loss, while other regions show a rapid (several ms) rise during the final loss, followed by a slow (~100 ms) decay. We interpret the slow rising signals, Fig. 8(c), as being dominated by plasma IR emission (e.g., Ar-I lines emitting in the 3–5 μm range) rising during the downward motion of the plasma and then disappearing when the plasma disappears. We interpret the fast rising signals, Fig. 8(d), as being due to localized RE heat loads, which cause a rapid rise and subsequent slow decay of surface temperature.

The rise and decay of RE surface heating can be well fit by a simple 1D thermal diffusion model, as shown by the dashed black line in Fig. 8(d). The IR brightness data are first corrected for plasma IR emission; this is done by assuming that the typical shape of the IR time trace from regions of the image dominated by plasma IR emission applies to all divertor regions. This typical plasma IR shape time trace is then scaled to match the pre-final loss signal and subtracted off to produce a corrected RE heating trace, red curve in Fig. 8(d). The 1D thermal diffusion model assumes a mono-energetic electron beam with some energy W_0 and pitch angle θ. The electron flux is assumed to have a step function time history, turning on at the start of the final loss and turning off instantly at the end with a total time-integrated perpendicular heat flux q_0. Thermal properties of the wall are assumed to be those of room-temperature amorphous graphite. Power deposition is calculated using standard total (radiative plus

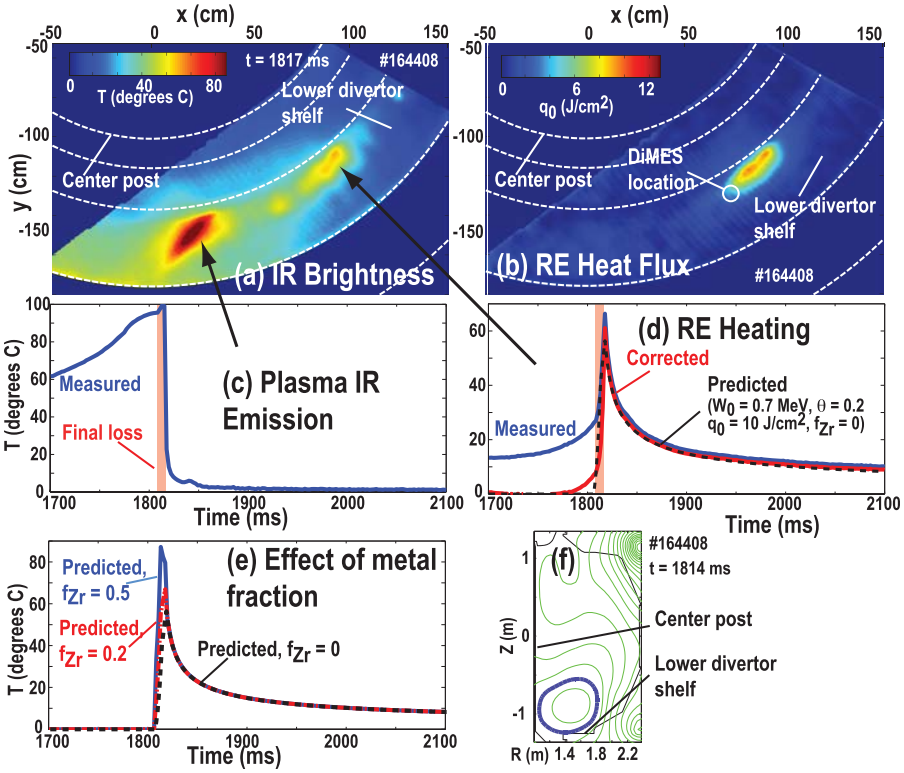

FIG. 8. IR thermography of a RE-wall strike showing: (a) image of divertor surface temperature at end of final wall strike; (b) image of resulting reconstructed RE heat flux; (c) temperature time trace at one point dominated by plasma IR emission; (d) temperature time trace at a different point dominated by RE heating; (e) effect of addition of Zr to graphite on predicted temperature time trace; and (f) JFIT magnetic flux contours showing position of RE beam during final loss.

collisional) stopping power curves for relativistic electrons. By varying W_0, θ, and q_0, excellent agreement with the data can be achieved, as shown by the black dashed line in Fig. 8(d). Unfortunately, these fits are not unique: changing W_0 and θ can have roughly similar effects on the shape of the temperature decay curve. It is therefore assumed that these unknown parameters lie within experimentally reasonable ranges $0.5\,\text{MeV} < W_0 < 5\,\text{MeV}$ and $0.05 < \theta < 0.2$ and error bars to q_0 are assigned based on fit errors within these allowed ranges.

Another possible complication of the thermography is the presence of trace metal in the divertor graphite due to experiments with the DiMES sample manipulator, which has been used to study sputtering of a wide range of metals, including Al, Mo, Zr, Ta, and W. Rutherford back scattering (RBS) and x-ray fluorescence (XRF) data indicate metals at a $\sim 10^{-4}$ concentration level with $\sim 100\,\text{nm}$ depth in the vicinity of DiMES (these experiments were conducted before the 2016 tungsten rings campaign which introduced significant additional tungsten). This small concentration is not expected to significantly alter the IR emissivity of the surface: this is supported by IR imaging of the TQ radiation flash in these experiments, which shows no enhanced signal in the vicinity of DiMES. Figure 8(e) shows the predicted effect of adding Zr, where f_{Zr} is the number density of Zr atoms divided by the number density of C atoms (we use Zr here as a rough representative metal atom). It can be seen that adding Zr significantly changes the peak temperature but has very little effect on the late time ($>50\,\text{ms}$ after the final loss) evolution. Also, significant concentrations ~ 0.5 are required to increase the peak surface temperature significantly. It therefore seems unlikely that local $\sim 10^{-4}$ concentration level metal deposits are responsible for the observed localized heating near DiMES. Nevertheless, to avoid any possible effect of metals, we fit to late time evolution $> 50\,\text{ms}$ to estimate q_0 across the lower divertor. A map of average q_0 across the divertor is shown in Fig. 8(b). As shown in the histogram of Fig. 7(a), this localized heating in the vicinity of $\phi = 150°$ is seen quite reliably in the IR imaging over many shots.

VI. KINETIC MODELING OF RE ENERGY DISTRIBUTION FUNCTION DURING FINAL LOSS

Measuring the energy and pitch angle distributions during the final loss is extremely difficult, so kinetic (test particle) modeling is used here to estimate the RE energy and pitch angle distribution functions during the final loss; these are then used to help interpret the HXR signals during the final loss. Reconstructions of f_E during the RE plateau can be made from data by combining soft x-ray (SXR), mid x-ray (MXR), HXR, Ar radiated power, and visible and IR synchrotron emission data.[16] To make the reconstruction of f_E tractable, a single pitch angle θ is assumed at each energy. These reconstructions have quite large error bars in the long-duration stationary plateau and are even more challenging to perform during the RE-wall strike because of the faster time scales, evolving plasma position, and mixing of wall and plasma signals. In order to estimate f_E during the final loss, we therefore begin with f_E reconstructed during the plateau from data, then integrate forward to steady-state using a simplified decoupled test particle simulation, and then finally integrate forward in time over the rapid final loss with a coupled test particle simulation.

The momentum evolution of a relativistic electron neglecting bremsstrahlung can be written as follows:[20]

$$\frac{\partial P}{\partial \tau} = \mu\hat{E} - \left(1+\frac{1}{P^2}\right) - FP\left(1-\mu^2\right)\left(1+P^2\right)^{1/2}, \quad (1a)$$

$$\frac{\partial P_{||}}{\partial \tau} = \hat{E} - \mu\left(1+\frac{1}{P^2}\right) - \mu\left(1+P^2\right)^{1/2}(1+Z)/P^2 - F\mu P^3\left(1-\mu^2\right)/\left(1+P^2\right)^{1/2}. \quad (1b)$$

In Eq. (1), $P \equiv p/m_e c$ is the normalized RE momentum, with $P_{||}^2 + P_{\perp}^2 = P^2$, and $\mu \equiv P_{||}/P = \cos\theta$, while $\tau \equiv t/\tau_c$ is time normalized by the (small angle) collision time $\tau_c = \frac{m_e c}{e E_{crit}}$. The dimensionless electric field is $\hat{E} \equiv E_\phi/E_{crit}$, where $E_{crit} = \left(e^3/4\pi\varepsilon_0^2 m_e c^2\right) n_e \ln\Lambda$ is the standard minimum (critical) electric field for RE formation. $F \equiv \upsilon_{rad}\tau_c$ represents the synchrotron radiation rate relative to the collision rate in the large radius of curvature limit valid in DIII-D, where $\upsilon_{rad} = \left(\frac{2r_e}{3c}\right)\omega_B^2$, with r_e the classical electron radius and $\omega_B = eB/m_e$ the electron gyrofrequency.

When the electric field is weak, $\hat{E} \lesssim Z$, Eq. (1) can be simplified by assuming that pitch angle equilibration occurs faster than energy evolution. In this decoupled time scale approximation, the pitch angle becomes[4]

$$\mu = \coth(\lambda) - 1/\lambda, \quad (2)$$

at all times, with

$$\lambda \equiv \frac{2\hat{E}}{1+Z}\left(\frac{\gamma^2-1}{\gamma}\right), \quad (3)$$

where γ is the standard Lorentz factor. The RE momentum evolution then becomes

$$\frac{\partial P}{\partial \tau} = \mu\hat{E} - \left(1+\frac{1}{P^2}\right) - \mu F\left(\frac{Z+1}{\hat{E}}\right)\left(\frac{1+P^2}{P}\right). \quad (4)$$

While we typically have $Z \sim 5$ and $\hat{E} \sim 5$ during the plateau, the electric field rises to $\hat{E} \sim 50$ during the final loss, so the decoupled time scale approximation Eqs. (2) and (4) breaks down. We therefore run the simpler Eq. (4) during the steady state (the plateau) only and then use the slower but more accurate Eq. (1) during the final loss.

To include secondary electrons, the Moller cross section is used.[21] The standard assumption that multiple small angle scatterings dominate drag, i.e., drag from the Moller cross section can be neglected in Eqs. (1) and (4), is used. The $1/K$ singularity (where K is the kinetic energy) in the Moller cross section is avoided by turning off Moller scattering into energies below 10 keV. Drift losses are approximated by causing particles with energy above the drift orbit scrape-off energy $K_X = m_e c^2 \frac{(a/2)}{\overline{q}\rho_{ec}}$ to be lost,[22] where $a \sim 0.25$ m is the RE beam minor radius, $\rho_{ec} = \frac{m_e c}{eB}$ is the RE gyroradius, and $\overline{q} \approx 2.5$ is used as a rough estimate for the mean RE beam safety factor. To avoid an unphysically sharp cutoff, a smooth cutoff ramp up of width 5 MeV is used. Particle trapping is coarsely approximated by turning off the electric field acceleration [the first term to the right of the equal sign in Eqs. (1) and (4)] for particles with large pitch angles $\sin\theta > \sqrt{b_{mirror}}$, where $b_{mirror} = \frac{B_{out}}{B_{in}} \approx 0.7$ is the mirror ratio.

Figure 9(a) shows examples of measured and simulated RE energy and pitch angle distribution functions during the plateau. The dashed black curve is the reconstructed f_E, near the start of the plateau. The gray shaded region represents uncertainty of this reconstruction. The dashed blue curve is the reconstructed f_E near the end of the plateau 240 ms later. It can be seen that the plateau energy distribution varies only slightly, i.e., a quasi-equilibrium is reached during the plateau. This is advantageous because RE formation during the TQ is quite complex and difficult to model,[23] but becomes unimportant here, since an equilibrium is reached. The plateau f_E is simulated by initializing with the measured f_E near the start of the plateau and then moving particle momenta between energy bins according to the decoupled test particle momentum equation, Eq. (4). The effect of different terms in the momentum equation is illustrated in Fig. 9(a) by sequentially adding terms. The magenta curve (i) contains only electric field and collisional drag. The green curve (ii) adds synchrotron drag. The orange curve (iii) then turns on secondary electron formation, and the red curve (iv) then adds in drift loss. It can be seen that the final (red) curve including all terms best matches the measured f_E. Drift loss appears to be most important for matching the high energy portion of f_E, while secondary electrons appear to be most important for matching the lower energy portion of f_E.

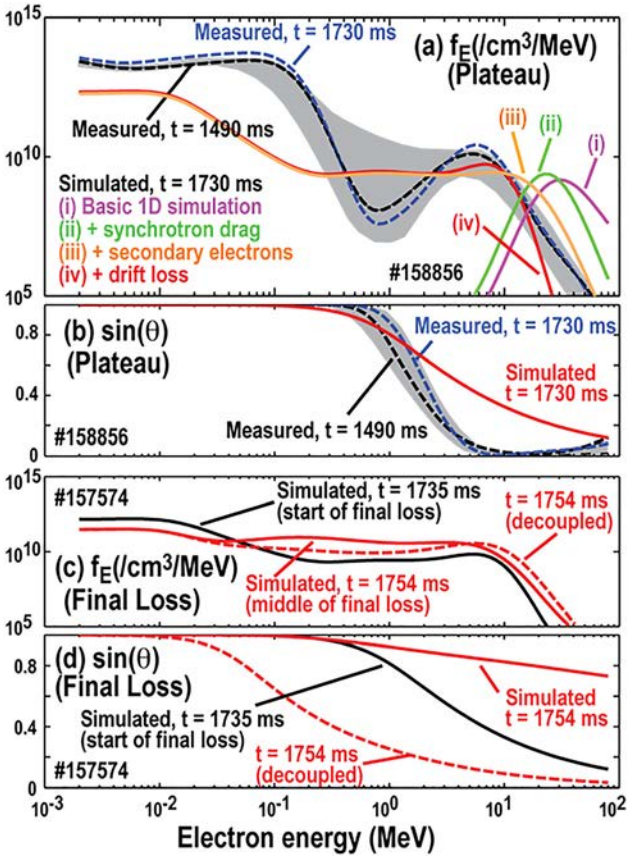

FIG. 9. (a) Measured and simulated RE energy distribution function during RE plateau showing effect of different drag/loss terms; (b) measured and simulated RE pitch angle during RE plateau; (c) simulated RE energy distribution function during final loss showing difference between coupled and decoupled models; and (d) simulated RE pitch angle during final loss. All curves are plotted as a function of electron kinetic energy.

Figure 9(b) shows (red curve) the simulated pitch angle distribution, Eq. (2), as a function of RE kinetic energy. Compared with the reconstructions (dashed curves), it can be seen that the general experimental trends (pitch angle rolling over around 1 MeV and decreasing toward zero) are captured by the simulation.

Figure 9(c) shows f_E simulated during the final loss: the black curve shows the start of the final loss and the red curves show the middle of the final loss. The dashed red curve shows the decoupled model, Eqs. (2) and (4), and the solid red curve shows the coupled model, Eq. (1). It can be seen that the two models differ only moderately during the final loss. Both predict a slight hardening (shift toward higher energy) of the f_E during the final loss. Figure 9(d) shows the pitch angle distribution predicted at the start (black curve) and middle (red curves) of the final loss. Here, it can be seen that the two models differ quite significantly: the decoupled model predicts a narrowing of the pitch angle (smaller pitch angle) during the final loss, while the coupled model predicts a broadening (larger pitch angle) during the final loss.

Overall, comparisons between measurements and modeling in Fig. 9 show that the test particle modeling can capture trends in the data but does not replicate the measurements perfectly, even within the large experimental error bars. We therefore estimate the conversion factor between final loss HXR signals and deposited kinetic energy using both (a) energy and pitch angle distribution functions measured during the plateau and (b) the distribution function simulated during the final loss, and then estimate error bars from the difference between the two. We define the HXR conversion factor V_S as the time-integrated HXR signal (in V-s, since HXR raw data are in V) divided by the total RE beam kinetic energy immediately prior to the final loss. Figure 10 shows the conversion factor V_S as a function of RE beam Z. Both simulated (triangles) and measured (circles) distribution functions are used. The solid curve shows the (logarithmic) average of the points, while dashed curves show the envelope of the points, used to estimate upper and lower error bars. Overall, within the large scatter, it can be seen that V_S depends only weakly on Z (if at all).

VII. RE ENERGY DEPOSITION AS A FUNCTION OF Z

Figure 11 gives an overview of the results on initial and deposited RE energy as a function of Z. Figure 11(a) shows

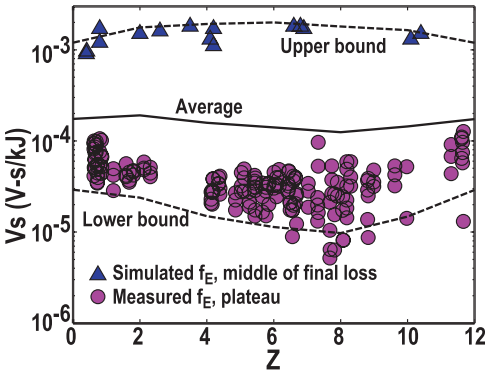

FIG. 10. Conversion factor to estimate RE deposited energy from HXR signals as a function of Z during final loss.

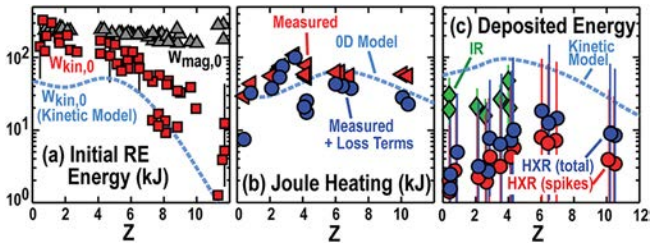

FIG. 11. (a) Initial RE energy (kinetic and magnetic); (b) Joule heating during the final loss; and (c) RE energy deposited into wall during final loss as a function of Z. Dashed curves show predictions of kinetic (test particle) models and 0D (coupled circuit) models.

initial (pre-final loss) RE beam energy: magnetic $W_{\mathrm{mag},0}$ and kinetic $W_{\mathrm{kin},0}$. The simulated $W_{\mathrm{kin},0}$ is shown as the dashed curve; this can be seen to typically be $\sim 5\times$ less than the measured $W_{\mathrm{kin},0}$, but still within the lower range of the large error bars in the data, shown as vertical lines on several points.

Figure 11(b) shows (red triangles) the Joule heating $I_{RE}V_0$ measured as described above and integrated over the final loss. It can be seen that this does not monotonically increase with Z but actually peaks at intermediate $Z \sim 6$. The increase in RE kinetic energy ΔW_{kin} during the final loss is expected to be the Joule heating minus any loss terms. Joule heating with loss terms estimated by the kinetic equation is shown by circles; it can be seen that this is typically a small correction (less than factor 2). For mid to high Z, isotropic (UV) line radiation is expected to be the dominant loss term. It was attempted to measure total radiated power during the final loss in these experiments, but a clear measurement was not obtained due to the small signal levels, slow time response of the slow (foil) bolometers, and high noise (due to HXRs) in the fast bolometers. An approximate upper bound of roughly 10 kJ was estimated, indicating a small effect. This is consistent with measurements on JET which concluded that radiation loss was small during the final loss[12] and is also consistent with the measurement of individual Ar lines, which rise only of order 20%–40% following final loss spikes, Fig. 6(c). The predicted Joule heating from the 0D model is $\Delta W_{kin} \approx W_{\mathrm{mag},0}/(1+\Re)$, where $\Re \equiv \frac{\tau_\Omega}{\tau_{Loss}}$.[6] This formula neglects loss terms during the final loss and assumes that $\tau_{Loss} \ll \tau_{Wall}$ (which is valid here). It can be seen in Fig. 11(b) that this matches the measurements fairly well. Here, we use the measured τ_Ω and measured τ_{Loss} (using $\tau_{Loss} = \tau_{HXR}/5$) to determine $\Re$.

Figure 11(c) shows the total deposited energy into the divertor during the final loss. The prediction of the kinetic model is shown by the dashed curve. Here, we use the predicted $W_{\mathrm{kin},0}$, add measured Joule heating, and subtract the (small) predicted loss terms predicted by the kinetic model. Measured $W_{\mathrm{kin},0}$ [shown in Fig. 11(a) but not in Fig. 11(c)] gives a model curve which is about 2–5× larger. Deposited energy predicted by HXR signals is shown by circles. The integral over HXR signals is done from the start of the final loss (when HXR signals rise, typically accompanied also by HXR flashes) until the end of the final loss (when HXR signals suddenly drop to zero). Toroidally averaged HXR

signals are used and the conversion factor of Fig. 10 as a function of Z is used to convert HXR signals to deposited energy (and assign error bars). Two different methods to separate wall HXR emission from plasma HXR emission during the final loss are used. HXR(total) assumes that the plasma HXR emission remains constant, subtracts pre-loss HXR level, and then integrates over the HXR signal during the final loss. This will tend to over-estimate the deposited energy, since some small rise in background (plasma) HXR emission could occur during the final loss due to wall impurity sputtering. HXR(spikes) only integrates HXR signals during final loss spikes. This will tend to under-estimate the deposited energy, since there could be some inter-spike RE loss to the wall (i.e., slower diffusive losses). Diamonds show the deposited energy estimated from IR thermography. In this case, error bars are assigned by assuming that energy and pitch angle lie in the range $0.5\,\mathrm{MeV} < W_0 < 5\,\mathrm{MeV}$ and $0.05 < \theta < 0.2$. Additionally, error bars are increased assuming either: (a) all the RE energy is deposited in the field of view (FOV) of the IR camera (lower bound) or (b) 1/6 of the RE energy is deposited in the FOV (which covers 60°). It is possible that the IR camera data upper error bars should be somewhat larger than this, if a large fraction of the RE energy is deposited outside of the camera FOV, as seems to be suggested by Fig. 7. IR camera data are not shown for $Z > 5$ because IR signals on these shots were too weak to analyze well. Overall, it can be seen that the kinetic model predicts the deposited energy within the scatter of the data for larger $Z > 5$ but tends to overestimate deposited energy for lower $Z < 5$ by a factor of about 5–10×.

VIII. CONCLUSIONS

This work was primarily motivated by the concern that RE plateaus with high impurity content (larger Z) would have higher Joule heating, possibly resulting in larger RE-wall damage in ITER if high Z injection is used to dissipate RE plateaus. However, the experiments indicate that RE loss time scale and Ohmic (resistive) time scale both vary with Z, leading to a ratio (and Joule heating) which actually peaks at intermediate $Z \sim 6$. The RE loss time scale is found to be close to the avalanche time; this suggests that the final loss time scale may be limited by the avalanche time. One potential mechanism for this would be that the final loss occurs at the rate at which the current channel can reform via secondary RE formation following loss spikes during MHD events. Despite the complex intermittent loss dynamics, the 0D model based on a simple diffusive RE loss appears to be reasonably good at predicting the total Joule heating averaged over the entire final loss event.

Efforts were made here to measure the total energy deposited on the wall by the REs, using HXR and IR signals. Both methods have large uncertainties, resulting in error bars of order a factor 10. Within these large uncertainties, the measured energy deposition appears to be consistent with predictions for larger $Z > 5$. At lower, $Z < 5$, however, the measured energy deposition appears to be significantly less than predicted. As seen in Fig. 11(c), the IR estimate for deposited energy is a factor of about 5 below predictions at low Z, but this could be accounted for if much of the deposition is consistently outside of the IR camera field of view. The HXR estimates for deposited energy in Fig. 11(c) are a factor of 10–20 below expectations, however, and cannot be explained by toroidal asymmetries, since the HXR array has reasonably good toroidal coverage. One possibility for this large discrepancy is that the initial RE beam kinetic energy is being overestimated at low Z. This seems unlikely though, since both the modeling and measurements are in rough agreement and it seems counterintuitive that the initial kinetic energy at low Z should be much lower than at high Z (which is more dissipative). A more likely explanation is that the conversion factor V_s of Fig. 10 is being overestimated at low Z, resulting in a deposited energy estimate from HXR signals which is too low. The conversion factor depends on many model-dependent steps, including the evolution of the energy and pitch angle distribution functions during the final loss, and the transmission of HXR signals through the vessel walls into the detector array. One possible source of significant error is the RE loss term used in the kinetic model. For example, the present model makes a very rough approximation for RE loss to the wall assuming this is dominated by drift orbit losses. However, an additional diffusive transport loss term could significantly affect the distribution function during the final loss, thus changing the conversion factor V_s.

Although this paper focuses on trends in RE Joule heating and energy deposition with Z, interesting results on the structure of RE-wall interaction are also observed. The toroidal structure of the HXR signals suggests a fairly broad interaction region globally, although the toroidal resolution of the diagnostic is fairly poor. The phase of the interaction does not appear to be random; instead, preferred loss phases are observed. In contrast, IR thermography indicates a fairly localized heat deposition in the vicinity of $\phi = 150°$, at least over the observed ∼60° window of coverage. It is possible that this increased local heat deposition in the vicinity of 150° might be due to metal deposits there, but this does not seem consistent with the very small ($\sim 10^{-4}$) metal concentrations measured with RBS and XRF. It seems that a more likely explanation seems to be that the DiMES port or some other fixed metal structure or field error is causing a preferential locking of the RE current channel phase during the final loss.

One caveat of this work is that the RE plateaus were kept under current and position control, i.e., an external loop voltage was applied to maintain plasma current constant up to the moment of the final loss. In an uncontrolled disruption in ITER, this high additional loop voltage drive would not exist, possibly resulting in a quite different energy distribution function. Future experiments are expected to investigate the vertical loss and energy distribution function evolution in uncontrolled RE plateaus. This situation is less controlled experimentally and thus more difficult to diagnose, but also more close to an actual uncontrolled RE beam scenario in ITER.

ACKNOWLEDGMENTS

The valuable diagnostic support of D. Ayala, M. van Zeeland, A. Briesemeister, E. Unterberg, J. Kulchar, and A. Moser is gratefully acknowledged. The sharing of XRF and

RBS results by C. Chrobak is gratefully acknowledged. Interesting discussions with A. Boozer are gratefully acknowledged. This work was supported in part by the U.S. Department of Energy under Nos. DE-FG02-07ER54917, DE-FC02-04ER54698, DE-AC05-00OR22725, DE-AC52-07NA27344, and DE-AC05-06OR23100 and in part by the Spanish Direccion General de Investigacion Cientifica y Tecnica under Projects ENE2012–31753 and ENE2015-66444R (MINECO/FEDERE, UE). DIII-D data shown in this paper can be obtained in digital format by following the links at https://fusion.gat.com/global/D3D_DMP.

[1]R. Nygren, T. Lutz, D. Walsh, G. Martin, M. Chatelier, T. Loarer, and D. Guilhem, J. Nucl. Mater. **241**, 522 (1997).
[2]G. F. Matthews, B. Bazylev, A. Baron-Wiechec, J. Coenen, K. Heinola, V. Kiptily, H. Maier, C. Reux, V. Riccardo, F. Rimini, G. Sergienko, V. Thompson, A. Widdowson, and JET Contributors, Phys. Scr. **T167**, 014070 (2016).
[3]T. C. Hender, J. C. Wesley, J. Bialek, A. Bondeson, A. H. Boozer, R. J. Buttery, A. Garofalo, T. P. Goodman, R. S. Granetz, Y. Gribov, O. Gruber, M. Gryaznevich, G. Giruzzi, S. Guenter, N. Hayashi, P. Helander, C. C. Hegna, D. F. Howell, D. A. Humphreys, G. T. A. Huysmans, A. W. Hyatt, A. Isayama, S. C. Jardin, Y. Kawano, A. Kellman, C. Kessel, H. R. Koslowski, R. J. La Haye, E. Lazzarus, Y. Q. Liu, V. Lukash, J. Manickam, S. Medvedev, V. Mertens, S. V. Mirnov, Y. Nakamura, G. Navratil, M. Okabayashi, T. Ozeki, R. Paccagnella, G. Pautasso, F. Porcelli, V. D. Pustovitov, V. Riccardo, M. Sato, O. Sauter, M. J. Schaffer, M. Shimada, P. Sonato, E. J. Strait, M. Sugihara, M. Takechi, A. D. Turnbull, E. Westerhof, D. G. Whyte, R. Yoshino, H. Zohm, and the ITPA MHD Topical Group, Nucl. Fusion **47**, S128 (2007).
[4]E. M. Hollmann, P. B. Aleynikov, T. Fulop, D. A. Humphreys, V. A. Izzo, M. Lehnen, V. E. Lukash, G. Papp, G. Pautasso, F. Saint-Laurent, and J. A. Snipes, Phys. Plasmas **22**, 021802 (2015).
[5]E. M. Hollmann, M. E. Austin, J. A. Boedo, N. H. Brooks, N. Commaux, N. W. Eidietis, D. A. Humphreys, V. A. Izzo, A. N. James, T. C. Jernigan, A. Loarte, J. Martin-Solis, R. A. Moyer, J. M. M. Burgos, P. B. Parks, D. L. Rudakov, E. J. Strait, C. Tsui, M. A. van Zeeland, J. C. Wesley, and J. H. Yu, Nucl. Fusion **53**, 083004 (2013).
[6]J. R. Martin-Solis, A. Loarte, E. M. Hollmann, B. Esposito, V. Riccardo, FTU and DIII-D Teams, and JET EFDA Contributors, Nucl. Fusion **54**, 083027 (2014).
[7]R. D. Gill, B. Alper, M. de Barr, T. C. Hender, M. F. Johnson, V. Riccardo, and EFDA-JET Contributors, Nucl. Fusion **42**, 1039 (2002).
[8]A. N. James, M. E. Austin, N. Commaux, N. W. Eidietis, T. E. Evans, E. M. Hollmann, D. A. Humphreys, A. W. Hyatt, V. A. Izzo, T. C. Jernigan, R. J. La Haye, P. B. Parks, E. J. Strait, G. R. Tynan, J. C. Wesley, and J. H. Yu, Nucl. Fusion **52**, 013007 (2012).
[9]M. Forster, K. H. Finken, M. Lehnen, O. Willi, Y. Xu, and the TEXTOR Team, Phys. Plasmas **19**, 052506 (2012).
[10]S. Putvinski, P. Barabaschi, N. Fujisawa, N. Putvinskaya, M. N. Rosenbluth, and J. Wesley, Plasma Phys. Controlled Fusion **39**, B157 (1997).
[11]J. Riemann, H. M. Smith, and P. Helander, Phys. Plasmas **19**, 012507 (2012).
[12]A. Loarte, V. Riccardo, J. R. Martin-Solis, J. Paley, A. Huber, M. Lehnen, and JET EFDA Contributors, Nucl. Fusion **51**, 073004 (2011).
[13]C. Reux, V. Plyusnin, B. Alper, D. Alves, B. Bazylev, E. Belonohy, A. Boboc, S. Brezinsek, I. Coffey, J. Decker, P. Drewelow, S. Devaux, P. C. de Vries, A. Fil, S. Gerasimov, L. Giacomelli, S. Jachmich, E. M. Khilkevitch, V. Kiptily, R. Koslowski, U. Kreuzi, M. Lehnen, K. Lupelli, P. J. Lomas, A. Manzanares, A. Martin de Aguilera, G. F. Matthews, J. Mlynar, E. Nardon, E. Nilsson, C. Perez von Thun, V. Riccardo, F. Saint-Laurent, A. E. Shevelev, G. Sips, C. Sozzi, and JET Contributors, Nucl. Fusion **55**, 093013 (2015).
[14]M. Lehnen, P. Aleynikov, D. Kiramov, V. Komarov, S. Konovalov, A. Loarte, J. Martinez, J. R. Martin-Solis, S. Maruyama, R. Mitteau, S. Pestchanyi, R. Pitts, B. Bazylev, R. Roccella, G. Saibene, J. Snipes, D. Campbell, S. Carpentier-Chouchana, P. de Vries, F. Escourbiac, Y. Gribov, G. Huijsmans, and R. Khayrutdinov, "Plasma disruption management in ITER," in IAEA Fusion Energy Conference, EX/P6-39, Kyoto, Japan (2016).
[15]J. L. Luxon, Nucl. Fusion **42**, 614 (2002).
[16]E. M. Hollmann, P. B. Parks, N. Commaux, N. W. Eidietis, R. A. Moyer, D. Shiraki, M. E. Austin, C. J. Lasnier, C. Paz-Soldan, and D. L. Rudakov, Phys. Plasmas **22**, 056108 (2015).
[17]A. H. Boozer and A. Punjabi, Phys. Plasmas **23**, 102513 (2016).
[18]S. M. Seltzer and M. J. Berger, Nucl. Instrum. Methods B **12**, 95 (1985).
[19]S. Agostinelli, J. Allison, K. Amako, J. Apostolakis, H. Araujo, P. Arce, M. Asai, D. Axen, S. Banarjee, G. Barrand, F. Behner, L. Bellagamba, J. Boudreau, L. Broglia, A. Bunengo, H. Burkhardt, S. Chauvie, J. Chuma, R. Chytracek, G. Cooperman, G. Cosmo, P. Degtharenko, A. Dellacqua, G. Epaola, D. Dietrich, R. Enami, A. Feliciello, C. Ferguson, H. Fesefeldt, G. Floger, F. Foppiano, A. Forti, S. Garelli, S. Giani, R. Giannitrapani, D. Gibin, J. J. Gomez, I. Gonzalez, G. Gracia, G. Greeniaus, W. Greiner, V. Grichnie, A. Grossheim, S. Guatelli, P. Gumplinger, R. Hamatsu, K. Hashimoto, H. Hasau, A. Heikkinen, A. Howard, S. Scherer, S. Sei, V. Sirotenko, D. Smith, N. Starkov, H. Stoecker, J. Sulkimo, M. Takahata, S. Tanaka, E. Tcherniaev, E. Safai, M. Tropeano, P. Truscott, H. Uno, L. Urban, P. Urban, M. Verderi, A. Walkden, W. Wander, H. Weber, J. P. Wellisch, T. Wenaus, D. C. Williams, D. Wright, T. Yamada, H. Yoshida, and D. Zschiesche, Nucl. Instrum. Methods **506**, 250 (2003).
[20]J. R. Martin-Solis, J. D. Alvarez, R. Sanchez, and B. Esposito, Phys. Plasmas **5**, 2370 (1998).
[21]C. Moller, Ann. Phys. **406**, 531 (1932).
[22]I. Entrop, "Confinement of relativistic runaway electrons in tokamak plasmas," Ph.D. thesis (Technische Universiteit Eindhoven, 1999).
[23]E. M. Hollmann, N. Commaux, R. A. Moyer, P. B. Parks, M. E. Austin, I. Bykov, C. Cooper, N. W. Eidietis, M. O'Mullane, C. Paz-Soldan, D. L. Rudakov, and D. Shiraki, Nucl. Fusion **57**, 016008 (2017).